Chemical equilibration of partons in high-energy heavy-ion collisions?

K. Geiger and J. I. Kapusta
School of Physics and Astronomy, University of Minnesota, Minneapolis, Minnesota 55455
(Received 12 January 1993)

The chemical composition of the hot and dense parton matter formed in the central region of ultrarelativistic heavy-ion collisions is studied for the case of Au+Au collisions at energies reached at the BNL RHIC using the parton cascade model. It is shown that within this framework, which is based on current understanding of semihard and hard interactions in QCD including the emission and absorption of soft partons, a chemical equilibration between the gluons and the quarks cannot be achieved. The gluons and u, d, s, and c quarks all rapidly approach kinetic equilibrium with a common temperature. The gluons subsequently also achieve chemical equilibrium, but the light quarks only reach about 60% of their ideal chemical equilibrium densities. It is demonstrated that the baryon density in the central region is small relative to the total parton density, with an associated ratio of baryon chemical potential to temperature of 0.35, slowly decreasing with time. The implications of the formation of such a hot, gluon-dominated plasma for strangeness, charm, and dilepton production are discussed.

PACS number(s): 12.38.Mh, 12.38.Bx, 24.85.+p, 25.75.+r

I. INTRODUCTION

Ultrarelativistic heavy-ion collisions ($\sqrt{s} \geq 200A$ GeV) are expected to exhibit new phenomena associated with the microscopic dynamics of quarks and gluons in the hot, ultradense environment that may be created in the central collision region of these reactions. In particular, the increasingly important role of multiple minijet production [1, 2], with $\sqrt{s}$ and mass number A, and the cascading of partons associated with semihard parton interactions ($p_\perp \simeq 1$–3 GeV) [3, 4], are expected to lead to a very rapid materialization of quarks and gluons in the central collision region and eventually to the formation of a thermalized quark-gluon plasma (QGP) state [5]. One of the major goals of the experimental programs at the future heavy-ion colliders, the BNL Relativistic Heavy Ion Collider (RHIC) and the CERN Large Hadron Collider (LHC), is to detect evidence for the predicted QCD phase transition to a QGP. Of particular interest is the question whether the QCD phase, as established shortly after the initial nuclear contact through the materialization of partons, lasts long enough to evolve into a thermally *and* chemically equilibrated plasma of quark-gluon matter [6]. Therefore it is essential to learn about the time scales associated with the development of the matter from the first instant of collision, via a preequilibrium stage, towards a QGP. Furthermore, an understanding of the preequilibrium dynamics and the characteristic properties of a realistic QGP in terms of the gluon and quark composition is inevitable for finding unambiguous signatures that can be identified with the experimental particle detectors.

In the spirit, and as a continuation, of Refs. [7, 8], the purpose of this paper is to address the dynamics of the chemical parton composition by studying, within the *parton cascade model* [9], the space-time evolution of the parton distributions for the illustrative case of central Au+Au collisions at RHIC energy $\sqrt{s} = 200A$ GeV (A=197). A detailed description of this model and its kinetic approach to simulate ultrarelativistic nuclear collisions in six-dimensional phase space and time is presented in Refs. [4, 7–9]. We will not explain here the specific aspects of the parton cascade model, but refer the interested reader to these earlier works, in particular to Ref. [9]. The general concept of the approach can be briefly summarized as follows. In the parton cascade model ultrarelativistic nuclear collisions are described as the time evolution of the partons' phase-space distributions. The space-time development is formulated within renormalization-group improved QCD perturbation theory, embedded in the framework of relativistic transport theory. The dynamics of the dissipative processes during the early stage of the nuclear reactions is simulated as the evolution of multiple interwoven parton cascades associated with quark and gluon interactions. Each cascade is an arbitrarily complicated composition of elementary $2 \rightarrow 2$ parton-parton "collisions," $1 \rightarrow 2$ parton "decays," and $2 \rightarrow 1$ "fusion" processes. Therefore the model incorporates the possibility of detailed balance with respect to the various interaction processes—a feature which is essential when addressing the question of thermal and chemical equilibration. At the end of the perturbative QCD phase the hadronization is modeled as a recombination of the final-state partons to form color singlet clusters, followed by the fragmentation of these clusters into observable hadronic states [9].

Within this model framework the characteristics of the microscopic parton dynamics were studied in Ref. [7] and, as a continuation, the "macroscopic" thermodynamic properties of the parton system were investigated in Ref. [8] by carrying out a phase-space analysis based on statistical kinetic theory. The latter work led to the conclusion that the partons, after materializing due to frequent interactions, rapidly reach a state of thermal

equilibrium in the central collision region, with the matter subsequently evolving in close resemblance to the famous Bjorken scenario [10]. In this paper we go one step further and focus on two issues associated with the space-time development of the parton matter composition with respect to its admixtures of gluons and the various quark flavors.

(i) *Chemical equilibration among the parton species.* In addressing the space-time evolution of a QGP, once it has been formed in the central collision region, it is commonly assumed that the plasma is of ideal-gas nature and its particle composition in terms of the relative admixtures of quarks, antiquarks, and gluons is simply taken from the particle species' plasma degrees of freedom according to the equation of state of a perfectly equilibrated parton gas. The initial parton content in the incoming nuclei, however, is far from being ideally composed, so that it is not at all clear if the system of partons indeed has time enough to evolve to a state of chemical equilibrium, even if it thermalizes kinetically.

(ii) *Baryon density evolution in space-time.* In most studies of QGP dynamics in high-energy nuclear reactions the baryon number of the incoming nuclei is assumed to reside completely in the receding beam fronts after the nuclei have passed through each other and that the central region is ideally baryon-free. This convenient assumption greatly simplifies an analysis of the QGP evolution in terms of relativistic hydrodynamics [11, 12]. However, this rigid division into a baryon-rich and a baryon-free domain throughout the nuclear reaction is an approximation that remains to be tested. Although the total baryon number is necessarily conserved throughout the collision, its spatial and momentum distribution will clearly change with time, since the baryon number density, which is proportional to the surplus of quarks over antiquarks, will be smeared out due to the interactions among the partons.

Our essential conclusions concerning these topics, from the results presented in this work, are the following.

(i) Chemical equilibration among the parton species *cannot* be achieved in heavy-ion collisions at RHIC energy, although a kinetically equilibrated QGP can well be established. The time necessary to attain chemical equilibrium is longer than the duration of the hot and dense stage during which the partons interact most frequently. The matter cools and flows apart before the relatively rare chemical processes, which change the relative admixtures of gluons and quarks, can yield a detailed balance. This property is intimately connected with the structure of perturbative QCD: the large number of initial gluons in the nuclear structure functions and the strong dominance of gluon interactions that outnumber processes involving quarks by far, favor a rapid and intense gluon production. The conversion of gluons into quarks becomes significant only after the gluon density saturates to its maximum value. In fact, our results clearly support the "hot glue scenario" proposed by Shuryak [13], which is a two-stage equilibration consisting of fast thermalization of gluons followed by much slower equilibration of quarks. According to our results this latter cannot be reached within the time scales set by the reaction dynamics of heavy-ion collisions at $\sqrt{s} = 200A$ GeV.

(ii) The baryon density distribution evolves in such a way that the central collision region can to a good approximation be considered baryon-free. The baryon chemical potential associated with the initial u and d valence quarks is found to rapidly decrease with time to about 35–50 MeV per flavor. This small value results mainly from two facts. First, the valence quarks have harder initial momentum distributions than the gluons and sea quarks and have a larger probability to survive the reaction without being deflected or significantly slowed down. Second, the relative contribution from slower or scattered valence quarks to the total central density of partons is quickly overwhelmed by intense production of secondary gluons, quarks, and antiquarks. Therefore, the excess of quarks over antiquarks that remains in the central region becomes very small compared to the total number of quarks plus antiquarks.

The paper is structured as follows. In Sec. II the kinetic framework for calculating particle densities, energy densities, temperatures, etc., from the space-time evolution of the parton distributions is briefly reviewed, which is then applied to study the thermodynamic behavior of the parton system in Au+Au collisions at $\sqrt{s} = 200A$ GeV and its composition in terms of the gluon and quark admixtures. In Sec. III we investigate the dynamics of the "chemistry" between gluons and quarks in the central collision region of these Au+Au reactions and analyze the tempted approach to chemical equilibrium among the parton species by comparison with the behavior expected for a perfect QGP. The space-time development of the baryon number distribution is the subject of Sec. IV, where the absolute magnitude of the baryon density and the associated baryon chemical potential in the central region is estimated. Finally, Sec. V is devoted to a summary and a brief discussion of positive implications of our results for a possible experimental detection of a QGP formation.

II. SPACE-TIME EVOLUTION OF THE PARTON DISTRIBUTIONS

In the kinetic description of the parton cascade model all the information about the dynamical evolution of the many parton system is contained in the time-dependent single-particle distributions for the various parton species in six-dimensional phase space: $F_a(r,p)$. Here and in the following the notation is $r \equiv r^\mu = (t, \mathbf{r})$, $p \equiv p^\mu = (E, \mathbf{p})$, and natural units $\hbar = c = k_B = 1$ are employed throughout. The subscript a specifies the type of parton, $a = q_f, \bar{q}_f, g$ (quarks, antiquarks of flavor f, and gluons). The time evolution of the distribution functions is governed by a relativistic transport equation of the form ($\partial_\mu \equiv \partial/\partial r^\mu$)

$$p^\mu \partial_\mu F_a(r,p) = \sum_{\text{processes } k} I_a^{(k)}(r,p) \,, \tag{1}$$

with a collision kernel $\sum_k I_a^{(k)} \equiv \sum_k (I_a^{(k)\,\text{gain}} - I_a^{(k)\,\text{loss}})$ that includes the various processes k by which a parton of type a with four-momentum p at space-time point r may

be gained or lost in a phase-space volume $d^3p d^3r$ centered at $\mathbf{p}$ and $\mathbf{r}$ at time t. The collision kernel is a sum over Lorentz-invariant collision integrals that involve the matrix elements for the different kinds of interaction processes in which at least one parton of type a is involved. Its specific form is given in Ref. [7]. Integrating Eq. (1) over $\mathbf{p}$ yields the following rate equations, one for each parton species a:

$$\partial_\mu n_a^\mu(r) = R_a^{\rm gain}(r) - R_a^{\rm loss}(r) \equiv R_a(r) , \tag{2}$$

where

$$R_a(r) = \sum_{\text{processes } k} \int \frac{d^3p}{(2\pi)^3 E} I_a^{(k)}(r,p) \tag{3}$$

is the net gain rate for partons a. The local space-time-dependent parton currents n_a are given by [8]

$$n_a^\mu(r) = \gamma_a \int \frac{d^3p}{(2\pi)^3 E} p^\mu F_a(r,p) . \tag{4}$$

The factors γ_a are the products of spin and color degeneracy, $\gamma_g = 2\times 8$ for gluons, and $\gamma_q = \gamma_{\bar q} = 2\times 3$ for quarks and antiquarks. We define the total parton current by summing over all species:

$$n^\mu(r) = \sum_{a=g,q_f,\bar q_f} n_a^\mu(r) . \tag{5}$$

Correspondingly, the energy-momentum tensor and the total entropy current of the parton system are

$$T^{\mu\nu}(r) = \sum_{a=g,q_f,\bar q_f} \gamma_a \int \frac{d^3p}{(2\pi)^3 p^0} p^\mu p^\nu F_a(r,p), \tag{6}$$

$$s^\mu(r) = -\sum_{a=g,q_f,\bar q_f} \gamma_a \int \frac{d^3p}{(2\pi)^3 p^0} p^\mu \{F_a(r,p)\ln[F_a(r,p)] - \theta_a [1+\theta_a F_a(r,p)]\ln[1+\theta_a F_a(r,p)]\} , \tag{7}$$

where $\theta_g = +1$ and $\theta_q = \theta_{\bar q} = -1$ take into account Bose-Einstein statistics for gluons and Fermi-Dirac statistics for quarks and antiquarks, respectively (note that $\theta_a = 0$ recovers the classical Maxwell-Boltzmann limit). From Eqs. (4)–(7) invariant scalars of particle density, pressure, energy density, and entropy density are obtained [14] by contracting with the local flow velocity

$$u^\mu(r) = n^\mu(r)/\sqrt{n_\nu(r) n^\nu(r)} , \tag{8}$$

so that

$$\begin{aligned} n(r) &= n_\mu(r)\, u^\mu(r), \\ p(r) &= -\tfrac{1}{3} T_{\mu\nu}(r)\,[g^{\mu\nu} - u^\mu(r) u^\nu(r)], \\ \varepsilon(r) &= T_{\mu\nu}(r)\, u^\mu(r) u^\nu(r), \\ s(r) &= s_\mu(r)\, u^\mu(r) , \end{aligned} \tag{9}$$

where $g^{\mu\nu} = \mathrm{diag}(1,-1,-1,-1)$. These quantities can be measured in the local rest frame of the matter where $u^\mu = (1,\mathbf{0})$. The total number, free energy, and entropy of the particles at a given time can be obtained by integrating over coordinate space.

At this point it is important to remark that for the following analysis we will take into account exclusively the real particles with $p^2 = M^2 \geq m_a^2$, where the m_a denote the species-dependent rest masses which are taken to be $m_u = 5.6$ MeV, $m_d = 9.9$ MeV, $m_s = 199$ MeV, $m_c = 1.35$ GeV, $m_b = 5$ GeV, and $m_g = 0$, and the quantity $M^2 - m_a^2$ measures the timelike virtuality of a parton. The term "*real*" partons is used for quanta which are either on mass shell or timelike; that is, the initial valence quarks as well as those partons that have been set "free" due to mutual interactions. Only these partons contribute to the entropy production and determine the multiplicities and relative abundances of the final observable hadrons. The "*virtual*" partons, on the other hand, are understood to be the remaining spacelike gluons and sea quarks with $p^2 \leq 0$ that represent the color field and the vacuum polarization.

To extract the parton distribution functions $F_a(r,p)$ in Eq. (1), which determine the particle currents via Eq. (2), at a given point of time during the nuclear collision, the six-dimensional phase-space volume is divided into cells k and the number $n_a(k)$ of partons of type a in each cell is counted. Statistics is improved by summing $n_a(k)$ over several collision events of the parton cascade simulation. The distribution functions $F_a(r,p)$ are then estimated as [8]

$$\bar F_a(k) = \frac{1}{\nu_{\rm ev}} \left(\frac{n_a(k)}{\Delta\Gamma_a(k)}\right) , \tag{10}$$

where $\nu_{\rm ev}$ is the number of collision events accumulated and

$$\Delta\Gamma_a(k) = \gamma_a \int_k \frac{d^3r\, d^3p}{(2\pi)^3} \tag{11}$$

is the phase-space volume of cell k in natural units ($\hbar = c = 1$) of the elementary volume $h^3 = (2\pi\hbar)^3 \equiv (2\pi)^3$ for partons of species a. The local densities n, ε, s, and pressure p are then computed in the local rest frame of the individual cells according to Eqs. (4)–(9) with $F_a(r,p) \to \bar F_a(k)$.

The characteristics of the partons' space-time evolution are depicted in Figs. 1–3. In Fig. 1 the parton distributions are shown at different proper times τ (defined below) along the longitudinal z axis, and in Fig. 2 along the transverse $r_\perp$ axis in the total center-of-mass frame of the colliding nuclei. Plotted are the numbers of par-

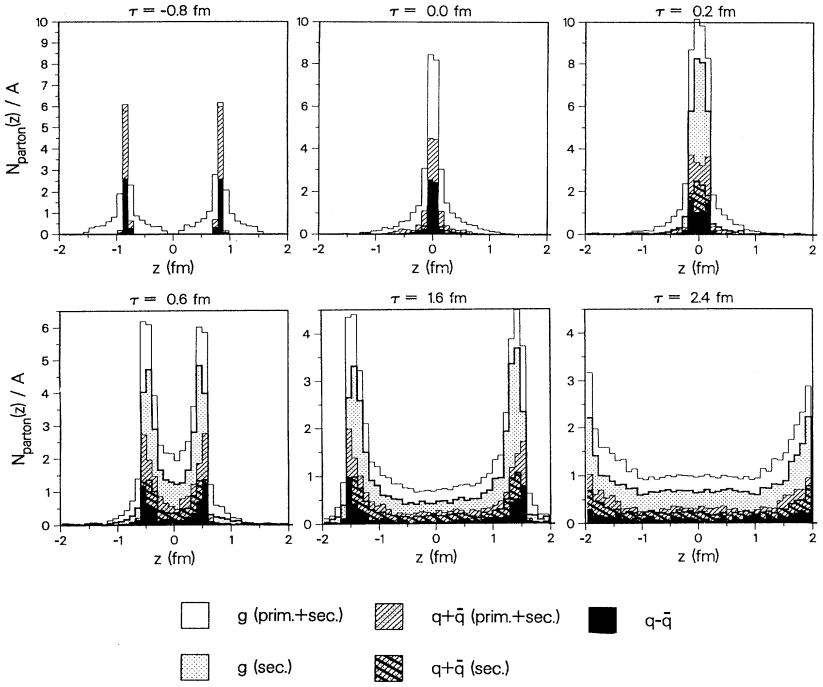

FIG. 1. Distributions of numbers of partons per nuclear mass number A in central Au+Au collisions ($A = 197$) at $\sqrt{s} = 200A$ GeV in the center-of-mass frame of the colliding nuclei at different times along the longitudinal z axis. The individual contributions from *virtual + real* (prim. + sec.) and from exclusively *real* (sec.) gluons and quarks, N_g/A, respectively $(N_q + N_{\bar{q}})/A$, are indicated by the various shaded areas, whereas the solid black areas display the valence quark distribution $(N_q - N_{\bar{q}})/A$, which is proportional to the baryon number distribution.

tons per nuclear mass number A in central Au+Au collisions ($A = 197$) at $\sqrt{s} = 200A$ GeV. The various shaded areas depict the contributions from virtual plus real and from exclusively real gluons, N_g/A, and from quarks plus antiquarks, $(N_q + N_{\bar{q}})/A$, whereas the solid black areas show the valence quark distribution $(N_q - N_{\bar{q}})/A$, which reflects the baryon number distribution. In Fig. 1 the initial state shows the two strongly Lorentz-contracted discs of valence quarks, surrounded by clouds of gluons and sea quarks. During the reaction an increasing number of these latter virtual quanta become real excitations due to multiple parton collisions and in addition new par-

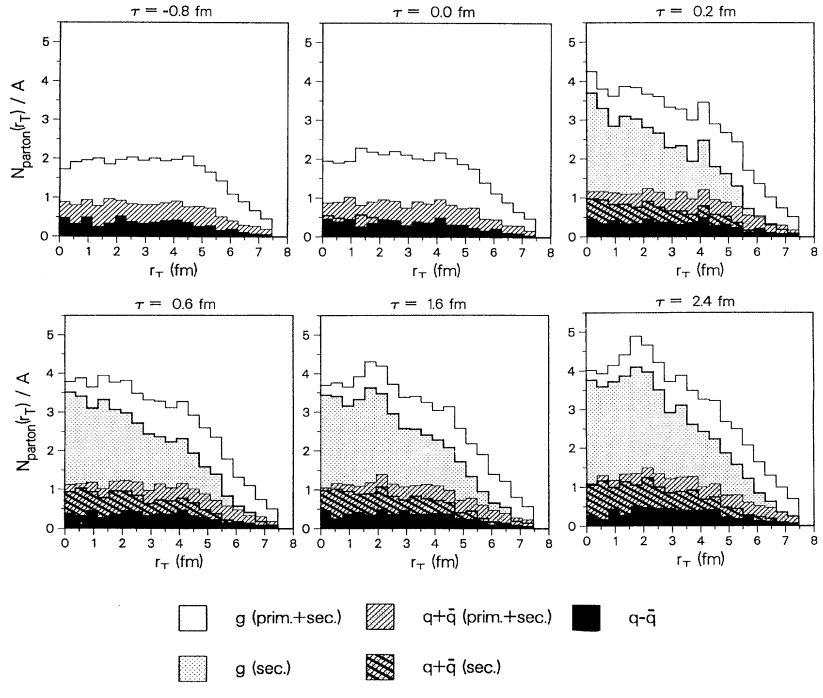

FIG. 2. Distributions of numbers of partons per nuclear mass number A along the transverse $r_\perp$ direction, corresponding to Fig. 1.

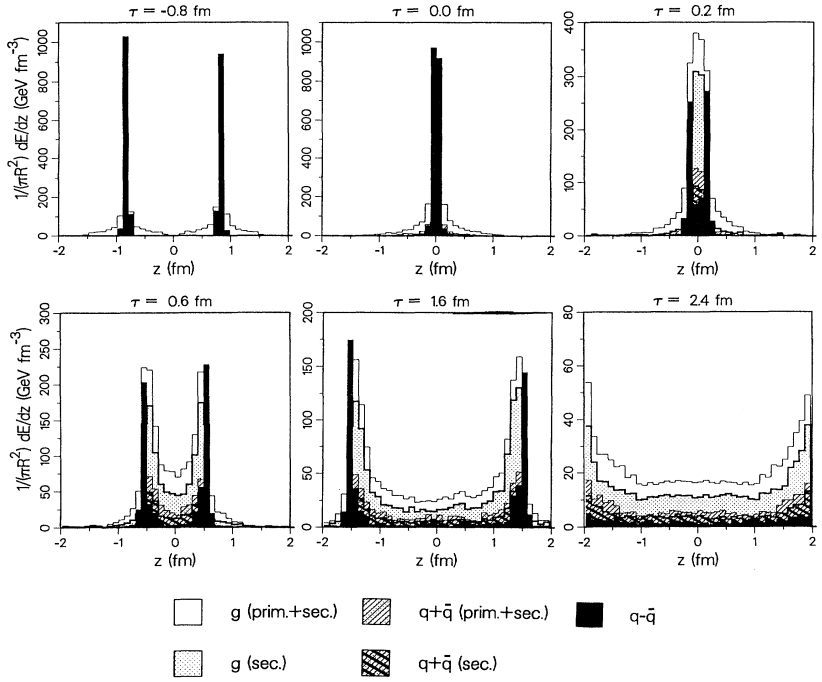

FIG. 3. Energy density distributions $\bar{\varepsilon}_g$, $\bar{\varepsilon}_q + \bar{\varepsilon}_{\bar{q}}$, and $\bar{\varepsilon}_q - \bar{\varepsilon}_{\bar{q}}$ [$\bar{\varepsilon} \equiv (\pi R^2)^{-1} dE/dz, R =$ 5 fm] at different times along the z axis, in correspondence to the parton distributions in Figs. 1 and 2.

ticles are created by gluon bremsstrahlung. By the time $\tau \simeq 2$ fm a rather homogeneous and isotropic plateau has developed, extending over the range $|z| \lesssim 1.5$ fm at $\tau = 2.4$ fm (the end of the calculation). The fast particles recede close to the speed of light as two beam fronts in opposite directions. Figure 2 demonstrates that the transverse distributions (initally reflecting the Fermi distributions of the nucleons in the incoming nuclei) become increasingly dense, but do not exhibit an appreciable radial expansion until at least $\tau = 2.4$ fm. Finally, Fig. 3 displays the time evolution of the energy density distributions $\bar{\varepsilon}_g$, $\bar{\varepsilon}_q + \bar{\varepsilon}_{\bar{q}}$, and $\bar{\varepsilon}_q - \bar{\varepsilon}_{\bar{q}}$ along the z axis, where $\bar{\varepsilon} \equiv (\pi R^2)^{-1} dE/dz$ ($R = 5$ fm), in correspondence to the parton distributions shown in Figs. 1 and 2. (Note that $\bar{\varepsilon}$ is *not* the proper energy density ε.) Figures 1–3 illustrate qualitatively the general features of the nuclear reaction dynamics that were already found in Refs. [7, 8]: Shortly after the nuclei interpenetrate, the partons in the central collision region materialize rapidly into real excitations due to very frequent interactions and, about $\tau \simeq 0.2$ fm after maximum overlap, already reach an approximate state of local thermodynamic equlibrium within a thin slab of width $\Delta z = 0.1$ fm around $z = 0$. As the matter expands longitudinally, it cools and becomes gradually distributed homogeneously over an increasing z range, and develops into a spatially macroscopic QGP with an isotropic momentum distribution. At $\tau = 2.4$ fm it has reached a volume of about 100 fm^3 centered at the overall center of mass with an effective temperature $T \simeq 300$ MeV.

For the following presentation it is convenient to use some phase-space variables appropriate for our analysis. We define the proper time τ as [8]

$$\tau = \mathrm{sgn}[t - t_0(s)] \sqrt{[t - t_0(s)]^2 - z^2} \,, \tag{12}$$

where t is the center-of-mass time and $t_0(s)$ is its value at the moment of maximum overlap of the colliding nuclei ($t_0 \simeq 0.8$ fm for $\sqrt{s} = 200A$ GeV, cf. Fig. 1). Thus, in the center of mass, at $z = 0$ fm, the initial nuclear contact occurs at $\tau \simeq -0.8$ fm and the maximum density is achieved at $\tau \simeq 0$. For the space-time variables we employ the space-time rapidity η and the transverse coordinate $\mathbf{r}_\perp$:

$$\eta = \ln\left(\frac{\tilde{t} + z}{\tau}\right) \,, \qquad r_\perp = \sqrt{x^2 + y^2} \,, \tag{13}$$

where $\tilde{t} \equiv t - t_0 \geq 0$. Thus, $r^\mu = (\tau \cosh\eta, \tau \sinh\eta, \mathbf{r}_\perp)$. The energy-momentum variables are described in terms of the usual rapidity y and the transverse mass $m_\perp$:

$$y = \ln\left(\frac{E + p_z}{m_\perp}\right) \,, \qquad m_\perp = \sqrt{p_\perp^2 + m^2} \,, \tag{14}$$

where $p_\perp = \sqrt{p_x^2 + p_y^2}$, so that

$$p^\mu = (m_\perp \cosh y, m_\perp \sinh y, \mathbf{p}_\perp).$$

Finally, we define the *central collision region*, for $\tau \geq 0$, as a cylindrical expanding volume bounded by

$$-1 \leq \eta \leq 1 \,, \qquad 0 \leq r_\perp \leq 5 \text{ fm} \,. \tag{15}$$

The following results were obtained by discretizing this central collision region into thin slabs of $\Delta z = 0.05$ fm and evaluating the parton distributions (10) and with these the thermodynamic quantities (9) according to Eqs.

(4)–(8) in the local rest frame of each slab.

In Fig. 4 the time development of the partons' momentum distributions in the central region (15) of Au+Au collisions at $\sqrt{s} = 200A$ GeV with zero impact is displayed, individually for gluons and the various quark flavors. Plotted are the invariant distributions

$$\frac{1}{\bar{n}_a}\frac{d\bar{n}_a}{d^3p}(\tau) = \frac{1}{(2\pi)^3}\frac{1}{\pi R^2 \Delta\eta} \times \int_{-\Delta\eta/2}^{\Delta\eta/2} d\eta \int_0^R d^2r_\perp \, F_a(\tau,\eta,r_\perp;y,m_\perp) , \tag{16}$$

versus $p \equiv |\mathbf{p}|$, which were obtained from the actual parton distributions $\bar{F}_a$ (10), averaged over the spatial volume defined by (15). Note that the histograms are scaled by powers of 10 for better presentation. The sequence of plots demonstrate that the partons indeed rapidly approach kinetic equilibrium in the central region, as is reflected by the increasingly thermal shape $\propto [\exp(E_a/T+\theta_a)]^{-1}$. The highly nonthermal initial momentum distribution [9] of the partons in the incoming nuclei first develops a power-law shape characteristic for the harder primary parton collisions and the associated (mini)jet production. With progressing time this QCD power-law tail flattens out and the exponential slope at lower momentum ($p \lesssim 3$ GeV), which is already visible at $\tau = 0.2$ fm, becomes steeper, indicating the decrease in the effective temperature of the system.

Figure 5 summarizes the thermodynamic properties of the system of partons implied by the time evolution of the phase-space distributions according to Eqs. (4)–(8). Shown are the pressure p, the densities n, ε, and s, as well as the associated temperature $T \equiv 4\varepsilon/(3s)$ as functions of the proper time τ (the curves are interpolations of the data points to guide the eye). The time dependence shown in Fig. 5 of the quantities n, p, ε, s, and T may be parametrized in terms of negative powers of τ/τ_0 with the parameter $\tau_0 = 0.05$ fm,

$$\begin{aligned} n(\tau) &= 565\ \text{fm}^{-3} \left(\frac{\tau}{\tau_0}\right)^{-0.90} , \\ p(\tau) &= 580\ \text{GeV fm}^{-3} \left(\frac{\tau}{\tau_0}\right)^{-1.25} , \\ \varepsilon(\tau) &= 1300\ \text{GeV fm}^{-3} \left(\frac{\tau}{\tau_0}\right)^{-1.15} , \\ s(\tau) &= 1800\ \text{fm}^{-3} \left(\frac{\tau}{\tau_0}\right)^{-0.85} , \\ T(\tau) &= 950\ \text{MeV} \left(\frac{\tau}{\tau_0}\right)^{-0.30} . \end{aligned} \tag{17}$$

At this point some explanatory remarks concerning these large densities and temperatures are appropriate. The densities n, ε, s, and consequently the temperature T are considerably higher than what one would expect from a simple estimate based on the number of primary hard parton-parton scatterings in pp collisions and extrapolating to AA reactions. In the parton cascade model

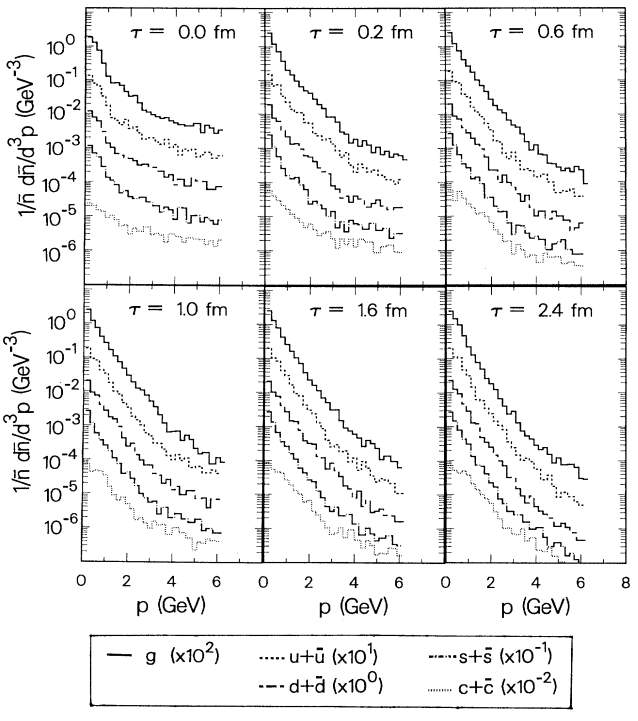

FIG. 4. Time development of the partons' momentum distributions in the central collision region (15) of Au+Au at $\sqrt{s} = 200A$ GeV from the moment of maximum overlap ($\tau = 0$) until the end of the calculations ($\tau = 2.4$ fm). Shown are the normalized distributions (16) for gluons and the different quark species. Note that the curves are multiplied by powers of 10 for better distinguishability.

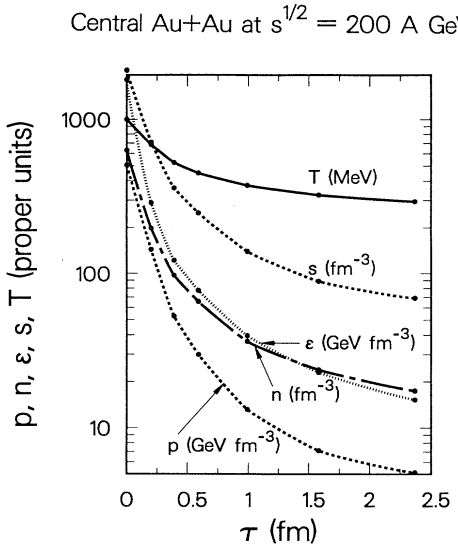

FIG. 5. Pressure p, particle density n, energy density ε, entropy density s, and associated effective temperature T of the system of partons in the central collision region (15) as a function of proper time τ in Au+Au collisions at $\sqrt{s} = 200A$ GeV and zero impact.

the intense production of secondary partons in AA collisions relative to pp collisions arises essentially from two sources. First, the probability of multiple scatterings per nucleon (either simultaneous scatterings of several partons of the same parent nucleon, or several successive secondary collisions of an individual parton), increases strongly with mass number A, i.e., the size of the nuclear system. Second, since each parton collision can initiate a cascade by emitting a number of radiative gluons from the scattered partons, the number of secondary partons multiplies rapidly, resulting in an increase of the phase-space density which in turn also increases the scattering probability of neighboring partons. For instance, whereas in pp collisions at $\sqrt{s} = 200$ GeV the average number of parton collisions with $p_\perp \geq 2$ GeV is calculated to be $n_{\rm scatt} \simeq 1.2$ per event, implying about $n^{\rm (sec)}_{\rm scatt} \simeq 0.2$ secondary scatterings, for central Au+Au collisions at $\sqrt{s} = 200A$ GeV the number of parton collisions turns out to be $n_{\rm scatt}/A \simeq 28$ per event, out of which $n^{\rm (sec)}_{\rm scatt}/A \simeq 13$ are secondary scatterings. Similarly, in pp collisions the number of produced gluons by radiative gluon emission is about $n^{(g)}_{\rm rad} \simeq 3$ per event, whereas in Au+Au it comes out to be already $n^{(g)}_{\rm rad}/A \simeq 25$. Therefore, in the parton cascade approach the large multiplicity of produced partons during the very early stage ($\tau \leq 0.5$ fm) of the nuclear collision when the longitudinal extent of the system is small, implies a high number density n and entropy density s. Connected with that is the harnessment of a considerable fraction of the initial beam energy which consequently leads to high energy densities ε.

Figures 6 and 7 exhibit the individual contributions of the different parton species to the particle densities and energy densities, respectively. Figure 6(a) shows the absolute magnitudes of the densities n_g, $n_q+n_{\bar q}$, and $n_q-n_{\bar q}$, summed over all quark flavors, as well as the total density of partons $n_{\rm tot}$ of the previous Fig. 5. Also plotted is the density of an ideal gas of noninteracting partons, $n_{\rm ideal} = 5.24\,T^3$, for three flavors of massless quarks and with the time-dependent temperature $T \equiv T(\tau)$ given in (17). These parton densities are not readily measured in a nucleus-nucleus collision, because of their transient nature. However, the observable particle ratios of final hadrons should reflect the quark flavor composition of the parton matter. Since the total amount of entropy produced by the partons in the central region during the preequilibrium stage reaches its final value when the system thermalizes [8] and remains a conserved quantity [10, 11] throughout the subsequent fluid dynamical expansion [12], the appropriate local measures of the quark flavor contents and the baryon density are the dimensionless ratios of the number densities $n_q + n_{\bar q}$ and $n_q - n_{\bar q}$, to the entropy density s of the whole system. Up to corrections due to final-state interactions, these ratios ought to be observable. For example, the strangeness content should be reflected in the kaon-to-pion ratio and the charm admixture to the relative abundance of the J/ψ, as well as D meson production. Figure 6(b) displays the ratios n_g/s and $(n_q + n_{\bar q})/s$ separately for the flavors $q = u,\ d,\ s,\ c$, as they evolve with time τ in the central region defined by (15). Similarly Fig. 6(c) shows the quantity $(n_q - n_{\bar q})/s$ for $q = u,\ d$, which reflects the time evolution of the central baryon density [note that $n_s - n_{\bar s}$ and $n_c - n_{\bar c}$ fluctuate locally, due to collisions involving primary s ($\bar s$) and c ($\bar c$) seaquarks, but are zero in the average]. In Fig. 7(a) the proper energy densities ε_g, $\varepsilon_q + \varepsilon_{\bar q}$ and the total-energy density $\varepsilon_{\rm tot}$ are plotted versus τ, in correspondence to the particle densities of Fig. 6. Again the time evolution of $\varepsilon_{\rm tot}$ compares remarkably well with the energy density $\varepsilon_{\rm ideal} = 15.63\,T^4$ of an ideal parton gas with three flavors of massless quarks and the temperature $T \equiv T(\tau)$ given in (17). The energy densities of the individual parton species are separately plotted in Fig. 7(b), ε_g and $\varepsilon_q + \varepsilon_{\bar q}$ for $q = u,\ d,\ s,\ c$, and in Fig. 7(c), $\varepsilon_q - \varepsilon_{\bar q}$ for $q = u,\ d$.

Although Figs. 6 and 7 imply that the parton matter in the central region behaves effectively like an ideal thermalized parton gas, it is evident that the composition of the matter in terms of the relative admixtures of gluons and quarks is strongly dominated by the former. Intense gluon production results in a matter composition in which the gluons make up almost 80% of the secondary partons and carry a correspondingly large fraction of the total energy and entropy. This feature is exhibited as a function of time τ in Fig. 8(a), in which the ratios of the different particle densities to the total density, $n_g/n_{\rm tot}$ and $(n_q + n_{\bar q})/n_{\rm tot}$, are shown. Figure 8(b),

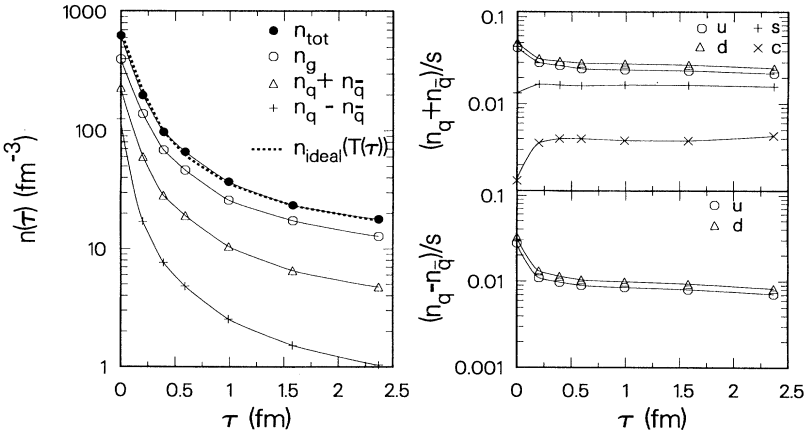

FIG. 6. (a) Time evolution of the central densities n_g, $n_q + n_{\bar q}$, and $n_q - n_{\bar q}$, summed over all quark flavors, as well as the total density of partons $n_{\rm tot}$ in Au+Au collisions at $\sqrt{s} = 200A$ GeV. Also displayed is the density of an ideal gas of noninteracting massless partons, $n_{\rm ideal}$, for three quark flavors and with the same temperature dependence as the actual parton densities from the cascade simulations. (b) Individual contributions of particle densities per unit entropy for gluons, n_g/s, and quarks plus antiquarks, $(n_q + n_{\bar q})/s$, for the flavors $q = u,\ d,\ s,\ c$. (c) The ratio $(n_q - n_{\bar q})/s$ for $q = u,\ d$ which reflects the time evolution of the central baryon density.

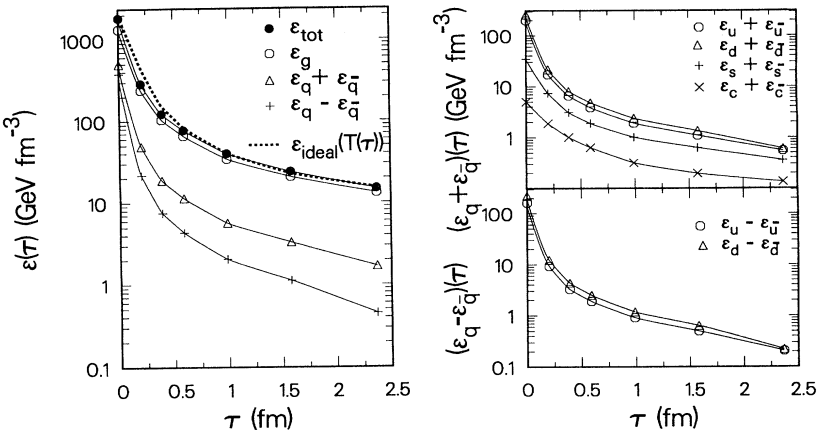

FIG. 7. (a) The central energy densities ε_g, $\varepsilon_q + \varepsilon_{\bar{q}}$, and the total-energy density $\varepsilon_{\rm tot}$ as a function of proper time τ, corresponding to the particle densities of Fig. 6. The density $\varepsilon_{\rm ideal}$ would be the energy density of an ideal parton gas with three flavors of massless quarks and with the same temperature as the actual energy densities obtained from the calculations. (b) Individual contributions ε_g and $\varepsilon_q + \varepsilon_{\bar{q}}$ for $q = u, d, s, c$ to the total-energy density of (a) from the various parton species. (c) The "baryonic" energy density $\varepsilon_q - \varepsilon_{\bar{q}}$ for $q = u, d$, associated with the surplus of quarks over antiquarks.

on the other hand, shows the relative abundances of the various quark flavors in the ratios $(n_q + n_{\bar{q}})/\sum_q (n_q + n_{\bar{q}})$ separately for $q = u, d, s, c$. In view of the naive expectation for the abundances of gluons and quarks, which one gets for an ideal quark-gluon plasma of massless noninteracting partons, $(n_g/n_{\rm tot})^{\rm (ideal)} = 0.37$ and $[(n_q + n_{\bar{q}})/n_{\rm tot}]^{\rm (ideal)} = 0.21$ (per flavor), it is clear that the results shown in Figs. 6–8 reflect a gluon plasma with a "contamination" of quarks. This property is a direct consequence of perturbative QCD [3, 13]: the average contributions to the collision rates (3), $R_a(ab \to bc)$, for the $2 \to 2$ processes, have ratios

$$R(gg \to gg) : R(gg \to q\bar{q}) \ : \ R(gq \to qg) \ : \ R(qq' \to qq') \ : \ R(q\bar{q} \to q'\bar{q}') \ : \ R(q\bar{q} \to gg)$$

$$= 30.9 \ : \ 0.58 \ : \ 17.3 \ : \ 2.3 \ : \ 0.12 \ : \ 0.14 \ , \quad (18)$$

so that the gg scattering significantly exceeds processes involving quarks. Similarly, the ratios of the $1 \to 2$ rates, $R_a(a \to bc)$, are

$$R(g \to gg) \ : \ R(g \to q\bar{q}) \ : \ R(q \to qg)$$

$$= 30.4 \ : \ 2.6 \ : \ 8.6 \ , \quad (19)$$

showing that the production of new partons in these processes is also strongly favoring the gluon yield. The time evolution of the total rates $R_g(\tau)$ and $R_q(\tau)$, according to Eq. (2), for the production of gluons and quarks (antiquarks), are shown in Fig. 9. In the next section we will analyze more quantitatively the thermodynamic properties of such a gluon-dominated parton matter and the consequences for the chemical equilibration process between the gluons and the various quark species.

III. DYNAMICS OF CHEMICAL EQUILIBRATION AMONG GLUONS AND QUARKS

The close resemblance between the time evolution of the central parton densities $n_{\rm tot}$ ($\varepsilon_{\rm tot}$) and the ideal densities $n_{\rm ideal}$ ($\varepsilon_{\rm ideal}$) in Fig. 6 (Fig. 7) indicates that the

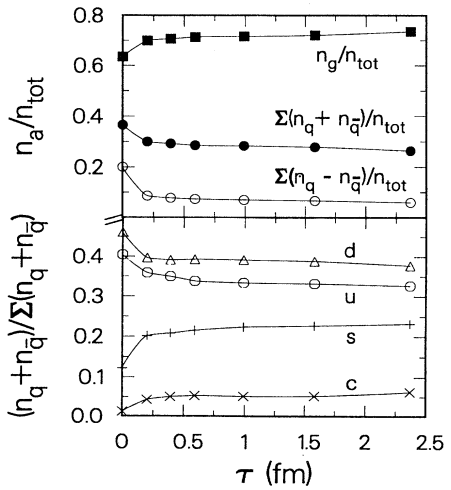

FIG. 8. (a) Time-dependent ratios of the different particle densities to the total density of partons, $n_g/n_{\rm tot}$ and $(n_q + n_{\bar{q}})/n_{\rm tot}$ in the central region (15) of Au+Au collisions at $\sqrt{s} = 200A$ GeV and zero impact. (b) Time evolution of the relative abundances of the various quark flavors in the ratios $(n_q + n_{\bar{q}})/\sum_q (n_q + n_{\bar{q}})$, separately for $q = u, d, s, c$.

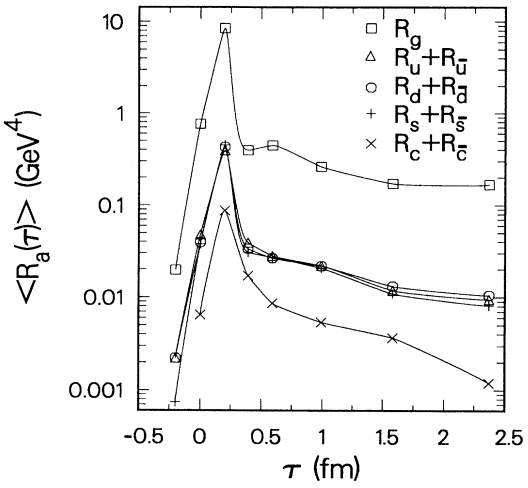

FIG. 9. Time dependence of the total rates $R_g(\tau)$ and $R_q(\tau)$ (averaged over the central region) for the production of a gluon and a quark (antiquark) of flavor $q = u, d, s, c$ in Au+Au collisions at $\sqrt{s} = 200A$ GeV.

matter produced in the central collision region quickly reaches a state of local kinetic equilibrium. In fact, it is evident from the collision rates displayed in Fig. 9 that by $\tau \simeq 0.2$ fm after the moment of maximum compression the most violent stage of parton-parton collisions is already over and the large longitudinally directed energy momentum has been stopped or redirected to a large extent. The subsequent interactions are mostly softer and result in an approximately isotropic momentum distribution of the partons. The system expands and cools very much as in the Bjorken model [10]. This behavior is a consequence of the fact that the parton distribution functions $F_a(r,p)$ in phase-space stabilize locally due to the rapid redistribution of energy momentum in the frequent parton interactions and particle production, at first around the overall center of mass at $z = 0$ fm and then with progressing time τ within an expanding cylindrical volume $\propto \tau$. Indeed, as is evident from Fig. 4, the actual distributions $F_a(r,p)$ approximately take the form of equilibrium distributions

$$F_a^{(\mathrm{eq})}(p,r) = \frac{1}{\exp[\beta_\nu(p^\nu - \lambda_a^\nu)] \pm 1} \quad , \tag{20}$$

where the upper sign refers to fermions (quarks) and the lower sign to bosons (gluons). The four-vectors $\lambda_\nu(r)$ and $\beta_\nu(r)$ are constructed from the local flow velocity $u_\nu(r)$, the local chemical potentials $\mu_a(r)$ (one for each parton species), and the inverse local temperature $\beta(r) = 1/T(r)$:

$$\lambda_a^\nu(r) = \mu_a(r) u^\nu(r) \quad , \tag{21}$$

$$\beta^\nu(r) = \beta(r) u^\nu(r) \quad . \tag{22}$$

The nonvanishing chemical potentials μ_a for species a are the parameters which measure the deviation from chemical equilibrium. In the local rest frame of the matter around the space-time point r the distributions $F_a^{(\mathrm{eq})}$ simplify to the energy distributions

$$F_a^{(\mathrm{eq})}(E,r) = \frac{1}{\exp\left[\frac{1}{T}(E-\mu_a)\right] \pm 1} \quad . \tag{23}$$

Note that the superscript "eq" refers to a kinetically equilibrated state of matter, which is not necessarily in chemical equilibrium. In the absence of any net baryon number or electric charge, perfect chemical equilibrium corresponds to $\mu_a = 0$ for all species a individually.

In order to gain more quantitative insight into the space-time-dependent thermodynamic behavior of the parton matter, we will in the following compare the parton densities resulting from the microscopic kinetics of the parton cascade simulation with the space-time evolution of an ideally mixed quark-gluon plasma at the same temperature. To do so, one first needs to calculate the relevant thermodynamic quantities of a perfectly equilibrated quark-gluon plasma, in correspondence to the actual densities computed on the basis of Eq. (4). Inserting the equilibrium distributions (20) into Eq. (4) and expanding the denominator of the integrand as a geometrical series, one gets, for the equilibrium particle density of parton species a at space-time point r,

$$\begin{aligned} n_a^{(\mathrm{eq})}(T,\mu_a) &= \frac{\gamma_a}{2\pi^2} m_a^2 T \sum_{j=1}^{\infty} \frac{(\theta_a)^{j-1}}{j} K_2\left(j\frac{m_a}{T}\right) \\ &\quad \times \exp\left(j\frac{\mu_a}{T}\right) \\ &\equiv \sum_{j=1}^{\infty} n_a^{(\mathrm{eq})}(j) \quad , \end{aligned} \tag{24}$$

where γ_a and θ_a are defined in Eq. (4), m_a is the invariant mass of the particles, and K_2 is the modified Bessel function of order 2. The total parton density is then

$$n^{(\mathrm{eq})}(T,\mu_a) = \sum_{a=g,q_f,\bar{q}_f} \sum_{j=1}^{\infty} n_a^{(\mathrm{eq})}(j) \quad . \tag{25}$$

For completeness we note the corresponding pressure, energy density, and entropy density, which are evaluated similarly,

$$p^{(\mathrm{eq})}(T,\mu_a) = \sum_{a=g,q_f,\bar{q}_f} \sum_{j=1}^{\infty} \frac{n_a^{(\mathrm{eq})}(j)}{j} T, \tag{26}$$

$$\begin{aligned} \varepsilon^{(\mathrm{eq})}(T,\mu_a) &= \sum_{a=g,q_f,\bar{q}_f} \sum_{j=1}^{\infty} \frac{n_a^{(\mathrm{eq})}(j)}{j} \\ &\quad \times \left(3T + m_a \frac{K_3(j\frac{m_a}{T})}{K_2(j\frac{m_a}{T})}\right), \end{aligned} \tag{27}$$

$$\begin{aligned} s^{(\mathrm{eq})}(T,\mu_a) &= \sum_{a=g,q_f,\bar{q}_f} \sum_{j=1}^{\infty} n_a^{(\mathrm{eq})}(j) \frac{1}{T} \\ &\quad \times \left(m_a \frac{K_3(j\frac{m_a}{T})}{K_2(j\frac{m_a}{T})} - \mu_a\right), \end{aligned} \tag{28}$$

where $n_a^{(\mathrm{eq})}(j)$ is defined in (24). The sums have to be evaluated numerically; however, they converge quite rapidly. Note that truncating the infinite sums after the first term ($j = 1$) corresponds to the classical Maxwell-Boltzmann limit.

In order to allow for an objective comparison between the ideal equilibrium quantities (24)–(28) and the actual parton densities given by Eqs. (4), (5), and (9), we require the same space-time evolution pattern for both. Furthermore, we make use of the result evident in Fig. 1, that transverse expansion effects of the matter can be neglected at least during the first few fm. Then all the thermodynamic quantities can be expressed as functions of the proper time τ only: $n(\tau, \mathbf{r}_\perp) = n(\tau)$, $p(\tau, \mathbf{r}_\perp) = p(\tau)$, $T(\tau, \mathbf{r}_\perp) = T(\tau)$, etc.

Figure 10 displays, as a function of time τ, the ratios of the total densities n and ε, Eq. (9), in the central region, resulting from the parton cascade simulation, to the corresponding equilibrium densities at temperature $T = T(\tau)$ and zero chemical potentials μ_a:

$$\rho^{(n)}(\tau) = \frac{n(\tau)}{n^{(\mathrm{eq})}(T,0)} \quad , \quad \rho^{(\varepsilon)}(\tau) = \frac{\varepsilon(\tau)}{\varepsilon^{(\mathrm{eq})}(T,0)} \quad . \tag{29}$$

Both $\rho^{(n)}$ and $\rho^{(\varepsilon)}$ reach unity (dotted line) after about $\tau \simeq 1$ fm, indicating that the actual particle and energy densities of the system as a whole show effectively the properties of an equilibrated parton gas [15]. Consistent with that is the time dependence of the dimensionless ratio $(\varepsilon/n)^{3/4}$, also shown in Fig. 10, which approaches the value of an ideal gas of gluons and quarks with N_f=3–4 quark flavors. However, from the previous considerations it is clear that the behavior exhibited by Fig. 10 is predominantly dictated by the gluon distributions and that the contributions of quarks and antiquarks to the total density are significantly below the values required for an ideal mixture among the various parton species. An indication for the establishment of a perfect chemical mixture would be that the ratios (29) tend to unity for gluons and each quark flavor *individually*.

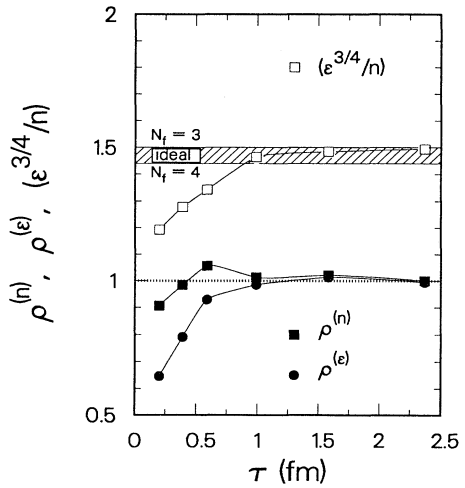

FIG. 10. Time evolution of the ratios $\rho^{(n)}$ and $\rho^{(\varepsilon)}$, Eq. (29), for the actual parton densities n and ε in the central region to the corresponding ideal equilibrium densities $n^{(\mathrm{eq})}$, respectively $\varepsilon^{(\mathrm{eq})}$, at the same temperature $T(\tau)$ obtained from the simulations of Au+Au collisions at $\sqrt{s} = 200A$ GeV. Also shown is the time dependence of the dimensionless ratio $(\varepsilon/n)^{3/4}$ in comparison to the value of an ideal gas of gluons and quarks with N_f=3–4 quark flavors.

To see how close the parton system comes to a complete chemical equilibrium, we have to compare separately for each species a the actual densities n_a and ε_a with the equilibrium densities $n_a^{(\mathrm{eq})}$ and $\varepsilon_a^{(\mathrm{eq})}$. To do so, we will take into account the fact that the momentum distributions of the parton species are rather distinct due to the difference in their masses and the frequency of their interactions. This property is reflected by Fig. 11(a), in which the time dependence of the average transverse mass $\langle m_{\perp a} \rangle = \langle \sqrt{p_{\perp a}^2 + m_a^2} \rangle$ is shown separately for the gluons and the different quark flavors. Also displayed for comparison is the quantity $\langle m_\perp^{(\mathrm{ideal})} \rangle \simeq \langle p_\perp^{(\mathrm{ideal})} \rangle = \sqrt{6}\,T$ which would be the average transverse mass (momentum) of massless partons in an ideal QGP with effective temperature $T \equiv T(\tau)$ (14). Obviously the gluons have a larger $\langle m_\perp \rangle$ than $\langle m_\perp^{(\mathrm{ideal})} \rangle$, whereas the u, d, and s quarks lie below the ideal curve and are approximately equal in magnitude. The c quarks have the largest $\langle m_\perp \rangle$ due to their large mass and the related fact that they are mostly produced in comparably large $p_\perp$ parton collisions. We can parametrize this distinctive property of the partons' momentum distributions by replacing the effective temperature T of the system as a whole with species-dependent "temperatures" T_a:

$$T(\tau) \longrightarrow T_a(\tau) = c_a^{-1} \, \langle E_a \rangle(\tau) \; , \tag{30}$$

where $\langle E_a \rangle = \varepsilon_a / n_a$ is the average energy per particle of type a in the local rest frame of the matter, and

$$c_g = \frac{\pi^4}{30\,\zeta(3)} \simeq 2.70, \qquad c_q = c_{\bar{q}} = \frac{7\pi^4}{180\zeta(3)} \simeq 3.15, \tag{31}$$

with the Riemann zeta function $\zeta(3) \simeq 1.202$. The resulting temperatures $T_a(\tau)$ are shown in Fig. 11(b) vs τ for gluons and the different species of quarks plus antiquarks, in comparison to the effective temperature $T(\tau)$, Eq. (17), of the parton system as a whole. The essential implication is that the quarks are noticeably cooler than the gluons.

Next, in accordance with (26), we define the ratios

$$\rho_a^{(n)}(\tau) = \frac{n_a(\tau)}{n_a^{(\mathrm{eq})}(T_a,0)} \quad , \quad \rho_a^{(\varepsilon)}(\tau) = \frac{\varepsilon_a(\tau)}{\varepsilon_a^{(\mathrm{eq})}(T_a,0)} \tag{32}$$

for each parton species $a = g, u, d, s, c$ separately. Figure 12 shows these ratios as functions of time τ. It is obvious that the system of partons *cannot* establish perfect chemical equilibrium with proper admixtures of gluons and quarks, although, as implied by Fig. 10, it exhibits the thermodynamic behavior of an ideal parton gas. The

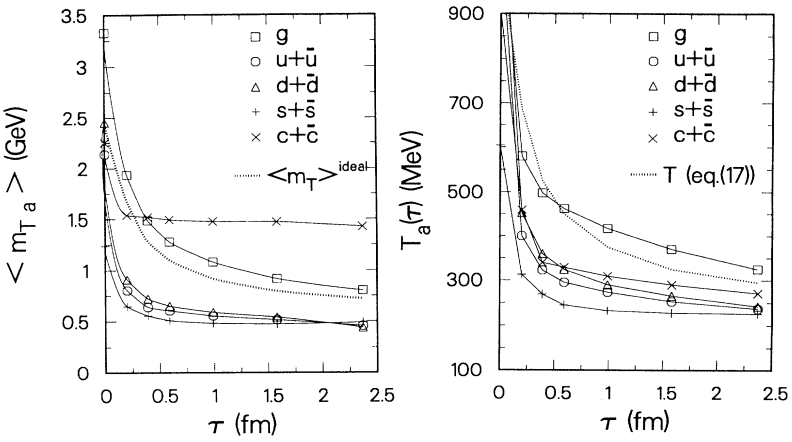

FIG. 11. (a) Average transverse mass $\langle m_{\perp a}\rangle = \langle\sqrt{p_{\perp a}^2 + m_a^2}\rangle$ of the gluons and the different quark flavors as a function of time in central Au+Au collisions at $\sqrt{s} = 200A$ GeV. The quantity $\langle m_\perp^{(\mathrm{ideal})}\rangle$ refers to average transverse mass (momentum) of massless partons in an ideal QGP with the same temperature dependence as the actual parton matter. (b) The different temperatures for gluons and the quark+antiquark species extracted from the average particle energies in the local restframe of the matter. The dotted curve is the extracted temperature of the parton system as a whole [Eq. (17)].

gluon density n_g, which rapidly increases and reaches its maximum around $\tau = 0.5$ fm, approaches to within 10% of its equilibrium value at about $\tau = 1.2$ fm. The densities of light quarks plus antiquarks, $n_q + n_{\bar{q}}$, buildup only to about 60% of their equilibrium densities [16]. The heavier quarks s and c achieve even less. An analogous conclusion holds for ε_g, $\varepsilon_q + \varepsilon_{\bar{q}}$ and $\varepsilon_q - \varepsilon_{\bar{q}}$. The dominance of the production of secondary gluons via $gg \to gg$, $gq \to gq$, as well as $g \to gg$ and $q \to qg$ [cf. (18), (19)], gives rise to a fast buildup of $\rho_g(\tau)$ which overshoots its equilibrium value. It bends over as the phase-space density reaches its maximum and gluon fusion (absorption) processes $gg \to q$, $qg \to q$ become significant. The further decrease of $\rho_g(\tau)$ is then mainly due to the diffusion of the quanta as the volume expands and the gluon density dilutes. The production of secondary quarks and antiquarks, on the other hand, does not occur fast and is intense enough to ensure an approach to chemical equilibrium because both type of processes, the conversion of virtual initial-state quarks to real excitations through $qg \to qg$, $qq' \to qq'$ and the production of new $q\bar{q}$ pairs through $gg \to gg$, $q\bar{q} \to q'\bar{q}'$, $g \to q\bar{q}$ are insufficiently frequent to compete with the dilution of the central densities as the plasma expands.

It is worth noting that as a consistency check we performed a calculation in which the quark-gluon coupling was artificially increased by replacing the QCD coupling strength $g_s \to 10\,g_s$ at these vertices ($g_s = \sqrt{4\pi\alpha_s}$), whereas the gluon-gluon coupling was kept at its proper value g_s. In this hypothetical case we find an enhanced production of quarks and antiquarks relative to the gluon yield such that the particle densities indeed come close to chemical equilibrium, with roughly equal relaxation times for both gluons and quarks.

The important conclusion from these considerations is that in heavy-ion collisions at $\sqrt{s} = 200A$ GeV the state of the parton matter formed in the central collision region clearly shows thermal properties, but cannot achieve full chemical equilibrium for the quarks. The state of matter is essentially a "gluon plasma" with a clear underrepresentation of quarks, rather than a QGP with proper chemical admixtures of quarks and gluons. Consequently the thermodynamic properties of the parton matter are dominated by the evolution of the gluon distributions. With increasing higher collider energy $\sqrt{s}$ this behavior may certainly change in favor of chemical equilibration,

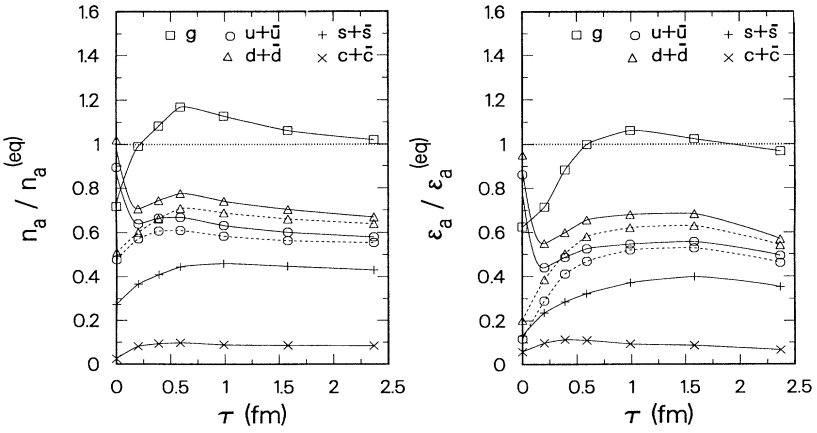

FIG. 12. Time development of the ratios (32), $\rho_a^{(n)}$ and $\rho_a^{(\varepsilon)}$, measuring the deviation of the actual particle and energy densities from their equilibrium values for gluons ($a = g$) and quarks plus antiquarks ($a = u, d, s, c$) in the central region of Au+Au collisions at $\sqrt{s} = 200A$ GeV. For u and d quarks the additional dashed lines represent the contributions of the secondary u, respectively d, quarks alone, i.e., without the already initially present valence quarks (except for those that have scattered at least once).

since the relaxation times of the parton densities decrease $\propto \ln s$ [8], so that a "perfect" QGP might be established at sufficiently high $\sqrt{s}$.

IV. BARYON DENSITY EVOLUTION

Finally we would like to address the question of how the baryon density evolves in space-time. As mentioned in the Introduction, it is usually assumed that its magnitude in the central region is negligible, so that this region of phase space can be considered as baryon-free. As it turns out, this is indeed a good approximation. The total baryon number of the system associated with the baryon content of the incoming nuclei must be conserved throughout the reaction. On the parton level, this translates to a constant total number of quarks minus antiquarks, with a surplus of $6A$ quarks in AA collisions (three per nucleon). However, the local baryon density $n^{(B)}$ changes with time (cf. Figs. 1 and 6). Since each quark carries a baryonic charge $+1/3$, it is given by

$$n^{(B)}(r) = \frac{1}{3} \sum_{a=u,d} \{n_a(r) - n_{\bar{a}}(r)\} \equiv \sum_{a=u,d} n_a^{(B)} , \qquad (33)$$

where n_a ($n_{\bar{a}}$) are the space-time-(r) dependent densities of u and d quarks (antiquarks) as before.

Qualitatively it is already evident in Fig. 1 that $\sum_a (n_a - n_{\bar{a}}) = 3n^{(B)}$ (indicated by the solid black histograms) is generally small relative to the total density of partons in the region between the receding beam fronts. Most of the baryon number resides in the beam fragmentation regions. The time evolution of $n_a - n_{\bar{a}}$ in the central collision region and of the associated baryonic energy densities $\varepsilon_a - \varepsilon_{\bar{a}}$ ($a = u, d$) is displayed in Figs. 6 and 7, which confirms the comparably small magnitude of $n^{(B)}$. Furthermore, Fig. 8 implies that already for $\tau \geq 0.2$ fm the ratio $\sum_a (n_a - n_{\bar{a}})/n_g$ is less than 0.1 and the ratio $\sum_a (n_a - n_{\bar{a}}) / \sum_a (n_a + n_{\bar{a}})$ is about 0.25.

In perfect chemical equilibrium one commonly defines a "baryon chemical potential" according to $\mu^{(B)} = \mu_u + 2\mu_d$, where $\mu_u = \mu^{(B)}/3 + 2\mu^{(Q)}/3$ and $\mu_d = \mu^{(B)}/3 - \mu^{(Q)}/3$, with $\mu_{\bar{u}} = -\mu_u$ and $\mu_{\bar{d}} = -\mu_d$. However, since we find that the system is evidently not in chemical equilibriums, the definition of a baryon chemical potential is somewhat ambiguous. Therefore, to extract a quantitative measure for the baryon density we infer an "effective baryon chemical potential" as it would be for a gas of massless u and d quarks. We proceed as follows. The chemical potentials μ_a introduced in the distribution functions (20) determine the deviation of n_a and $n_{\bar{a}}$ from their chemical equilibrium values, separately for quarks and antiquarks of flavor a. On the other hand, since the quantity $\rho_a^{(n)}$, introduced in Eq. (32), measures the degree of chemical equilibration of the sum $n_a + n_{\bar{a}}$, whereas the baryonic potential $\mu_a^{(B)}$ measures the difference $n_a - n_{\bar{a}}$, one can make a variable transformation

$$(\mu_a,\ \mu_{\bar{a}}) \longrightarrow (\rho_a^{(n)},\ \mu_a^{(B)}) \qquad (34)$$

with

$$\rho_a^{(n)} = \rho_{\bar{a}}^{(n)} , \qquad \mu_a^{(B)} = -\mu_{\bar{a}}^{(B)} , \qquad (35)$$

where the latter constraint on $\mu_a^{(B)}$ arises from the conservation of the total baryon number. The transformation (34) amounts to replacing the form (23) of the distribution functions by

$$F_a^{(\mathrm{eq})}(E, r) = \frac{\rho_a^{(n)}}{\exp\left[\frac{1}{T}(E - \mu_a^{(B)})\right] \pm 1} . \qquad (36)$$

Inserting these distributions into Eq. (4) and using the constraints (35) , the local baryon density (33) can be expressed in the form

$$n^{(B)}(r) = \frac{1}{18\pi^2} \sum_{a=u,d} \gamma_a \rho_a^{(n)} \{\mu_a^{(B)3} + \mu_a^{(B)} (\pi T)^2\} , \qquad (37)$$

where $\gamma_u = \gamma_d = 2 \times 3$ are the spin-color degeneracy factors and T is the effective temperature of the parton system. Solving for $\mu_a^{(B)}$ as a function of the baryon densities $n_a^{(B)}$, one obtains the individual contributions of u and d quarks to the baryon chemical potential:

$$\mu_a^{(B)} = \left[(3\pi)^2 \left(\frac{n_a^{(B)}}{\gamma_a \rho_a^{(n)}} \right) + \sqrt{(3\pi)^4 \left(\frac{n_a^{(B)}}{\gamma_a \rho_a^{(n)}} \right)^2 + \frac{(\pi T)^6}{27}} \right]^{1/3} + \left[(3\pi)^2 \left(\frac{n_a^{(B)}}{\gamma_a \rho_a^{(n)}} \right) + \sqrt{(3\pi)^4 \left(\frac{n_a^{(B)}}{\gamma_a \rho_a^{(n)}} \right)^2 - \frac{(\pi T)^6}{27}} \right]^{1/3} . \qquad (38)$$

With the calculated densities n_a and $n_{\bar{a}}$ ($a = u, d$) and the associated temperature T (14), resulting from the parton cascade simulation, one readily can estimate the time evolution of the baryon density through Eq. (37) [cf. Figs. 6(b) and 7(b)] and of the corresponding baryon chemical potential through Eq. (38). Figure 13(a) shows the absolute magnitudes of $\mu_a^{(B)}$ as a function of τ. It is about equal for both u and d quarks and decreases

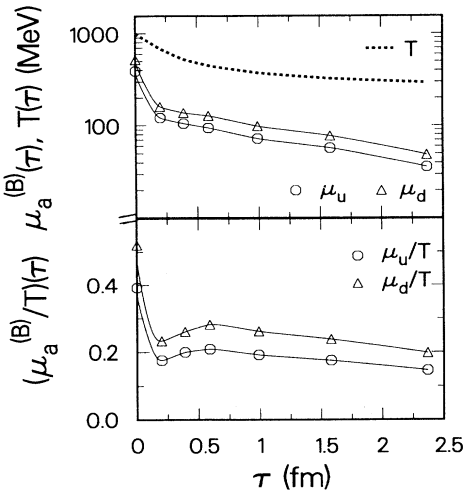

FIG. 13. (a) Baryon chemical potentials $\mu_a^{(B)}$ for $a = u, d$ as a function of time τ in the central region of zero-impact Au+Au collisions at $\sqrt{s} = 200A$ GeV. The dashed line shows for reference the temperature T (17) of the parton system as a whole. (b) Corresponding time development of the dimensionless ratio $\mu_a^{(B)}/T$ for u and d quarks at temperatures $T(\tau)$ of the total parton system.

rapidly from $\mu_{u(d)}^{(B)} \simeq 400\,(500)$ MeV at $\tau = 0$ to about $\mu_{u(d)}^{(B)} \simeq 35\,(50)$ MeV at $\tau = 2.4$ fm. Thus, the total $\mu^{(B)} = \mu_u^{(B)} + \mu_d^{(B)}$ amounts to roughly 90 MeV. Figure 13(b) displays the dimensionless ratios $\mu_a^{(B)}/T$ for u and d quarks separately, which at first relax fast (within $\simeq 0.5$ fm) and then decrease slowly to values of $\simeq$0.15–0.2 at $\tau = 2.4$ fm, or $\mu^{(B)}/T \simeq 0.35$. The spatial distribution of $\mu^{(B)}$ along the z axis at $\tau = 2.4$ fm turns out to be rather homogeneous in magnitude throughout the range $|z| \lesssim 1.8$ fm, in resemblance to the matter distribution of $\sum_a (n_a - n_{\bar{a}})$ shown in Fig. 1.

Finally, in Fig. 14 the rapidity distribution dN/dy and the transverse momentum distribution $dN/dp_\perp^2$ at the end of the calculations $\tau = 2.4$ fm of $\sum_q (N_q - N_{\bar{q}}) = 3N^{(B)}$ is shown in relation to the ones of N_g and $\sum_q (N_q + N_{\bar{q}})$ summed over all quark flavors. In Fig. 14(a) it is interesting to observe that although the baryon number distribution extends up to almost $y = 6$ due to those initial-state valence quarks that have not been much deflected or slowed down (the initial valence quark distributions are peaked around $y = 5.4$), a significant buildup of the baryon number in the initially sparsely populated central rapidity region $y \lesssim 2.5$ is visible, where also the majority of gluons and secondary quarks are produced. Figure 14(b) illustrates that the $p_\perp$ distribution of $\sum_q (N_q - N_{\bar{q}})$ is flatter and develops a stronger tail than the gluons or secondary quarks, because the valence quarks have a harder initial momentum distribution. Therefore, those valence quarks that undergo a primary collision obtain on the average a larger $p_\perp$ kick than gluons, sea quarks, or partons in secondary scatterings.

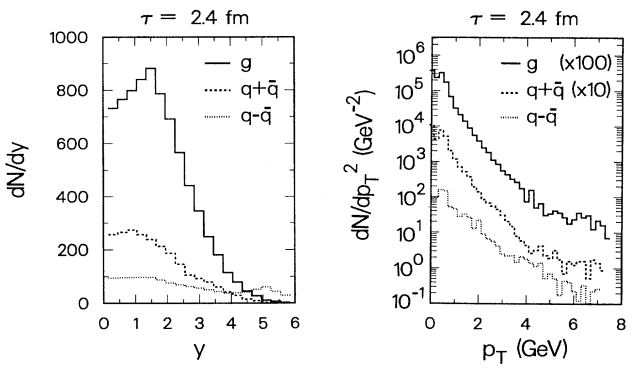

FIG. 14. (a) Rapidity distribution dN/dy of the secondary quarks ± antiquarks and gluons at $\tau = 2.4$ fm in central Au+Au collisions at $\sqrt{s} = 200A$ GeV. (b) Corresponding transverse momentum distribution $dN/dp_\perp^2$.

V. SUMMARY AND CONCLUSIONS

Within the framework of the parton cascade model, we have studied the composition of the parton matter formed in central Au+Au collisions at RHIC energies $\sqrt{s} = 200A$ GeV. The results from simulations of these reactions imply a rapid thermalization of the partons' phase-space distributions in the central collision region and the formation of a very hot and dense state of parton matter. Within this scenario we analyzed the "chemistry" of partons in terms of the contributions of gluons and the different quark flavors to the particle and energy densities. The essential results can be summarized as follows.

(i) The matter formed in the central region (with space-time rapidity $|\eta| \leq 1$) is essentially a hot gluon plasma rather than a quark-gluon plasma, with an effective temperature close to 1 GeV shortly after the moment of maximum nuclear overlap ($\tau = 0$). The dynamics is clearly dominated by the gluons.

(ii) As the system expands and cools, the gluon density reaches its equilibrium value around $\tau \approx 2$ fm. The densities of quarks and antiquarks always stay well below the gluon density and cannot build up to the full equilibrium values required for an ideal chemical mixture of gluons and quarks. The time for chemical equilibration of the quarks is too long to compete with the dilution of the densities due to expansion and cooling.

(iii) The baryon density in the central region, associated with the valence quarks, turns out to be generally small relative to the total parton density. The basic reasons for this are as follows: first, the valence quarks have a harder initial momentum distribution than the gluons and sea quarks, and second, the total parton density increases rapidly due to the intense materialization of initially virtual partons and the copious production of additional particles, whereas the baryon density is quickly diluted in the central region and resides mostly in the receding beam fronts. The central baryon density amounts

to less than 10% of the total parton density, which translates into an estimate of the associated baryon chemical potential $\mu^{(B)} \simeq 90$ MeV at $\tau = 2.4$ fm, or $\mu^{(B)} \simeq 0.35\,T$.

Clearly, these predictions rely on the validity of the parton cascade model and the underlying concept of describing the reaction dynamics of high-energy nuclear collisions and the thermalization properties of partons in terms of perturbative QCD. However, if the copious minijet production and the associated evolution of parton cascades are the essential driving forces of the microscopic dynamics, at least during the first few fm of the nuclear collision, then the properties of perturbative QCD and relativistic kinetic theory naturally result in a "hot glue" scenario as summarized in (i)–(iii). In this case [13], the consequences for observable QGP signatures [17, 18] would be rather positive.

(a) *Enhanced production of charm.* Although, as concluded, no chemical equilibration of charmed quarks can be achieved, direct charm production via $gg \rightarrow c\bar{c}$ is expected to be enhanced significantly during both the preequilibrium stage [19] and the QGP evolution [20], for which $c\bar{c}$ production by hot gluons strongly increases with the initial temperature T_i of the thermalized parton matter. For example, the thermal $c\bar{c}$ production rate was estimated [20] for central Au+Au collisions at RHIC to give per collision event about 1 $c\bar{c}$ for $T_i = 400$ MeV, 10 $c\bar{c}$ for $T_i = 550$ MeV, and already 100 $c\bar{c}$ for $T_i = 700$ MeV, which clearly exceeds the standard parton model predictions of about 0.8 $c\bar{c}$ without a QGP formation in these collisions [19, 20]. Therefore direct charm production is a very sensitive "thermometer" and could be an obvious signal for a QGP formation, if the experimental measurement of the charmed meson yield can cleanly be resolved. An additional source of charm production is related to the rising interaction probability of initial-state charmed sea quarks as the density of the matter increases, so that the production of open charm can give a further significant contribution to the total charm multiplicity [8].

(b) *Strangeness production.* The enhancement of total strangeness $s + \bar{s}$ [21, 22] depends on the interrelation of the strange quark mass m_s and the temperature T. For the hot and dense scenario predicted by the parton cascade simulations, even at $\tau = 2.4$ fm the temperature is still $T \simeq 300$ MeV, which is considerably larger than m_s and so there is no essential difference between initially produced u, d, and s quarks. If the multiple strange quark pairs, once produced, do not annihilate easily, there should be an enhanced strangeness production observable.

(c) *Lepton pair production.* The spectra of dileptons produced during the early stage of the parton cascade evolution do exhibit a rather different behavior than the spectra obtained in the thermal scenario [23]. In Ref. [24] the radiation of lepton pairs by the quarks during central collisions between gold nuclei at RHIC energy was calculated within the parton cascade model. It was found that the distribution of radiated pairs evolves smoothly from the initial Drell-Yan-type reactions all the way towards equilibrium radiation. Contributions from reactions involving "hot" secondary partons during the preequilibrium and thermal stage dominate the Drell-Yan yield by at least a factor of 5 even at an invariant mass of 8 GeV. Qualitatively similar results have been found in related analyses [25]. Therefore, experiments should be able to test the evolution of partons towards thermal equilibrium at these energies. The observable implications outlined above for the production of charm and strangeness as QGP signatures will be addressed quantitatively in a separate publication [26].

ACKNOWLEDGMENTS

The parton cascade simulations were performed on the Cray computers of the Minnesota Supercomputer Institute and on a Silicon Graphics computer at Duke University (an opportunity for which we thank B. Müller). This work was supported by the U.S. Department of Energy under Contract No. DOE/DE-FG02-87ER-40328.

[1] X.-N. Wang, Phys. Rev. D **43**, 104 (1991).
[2] K. Kajantie, P. V. Landshoff, and J. Lindfors, Phys. Rev. Lett. **59**, 2527 (1987); K. J. Eskola, K. Kajantie, and J. Lindfors, Nucl. Phys. **B323**, 37 (1989).
[3] E. M. Levin and M. G. Ryskin, Phys. Rep. **189**, 267 (1990); L. V. Gribov, E. M. Levin, and M. G. Ryskin, *ibid.* **100**, 1 (1983).
[4] K. Geiger and B. Müller, Nucl. Phys. **B369**, 600 (1992).
[5] For an overview, see *Quark Matter '91*, Proceedings of the Ninth International Conference on Ultrarelativistic Nucleus-Nucleus Collisions, Gatlinburg, Tennessee, 1991, edited by T. C. Awes *et al.* [Nucl. Phys. **A544**, 1c (1992)].
[6] A recent paper addressing the problem of parton equilibration, very much related to our paper, is by T. S. Biro, E. van Doorn, M. H. Thoma, B. Müller, and X.-N. Wang, "Parton Equilibration in Ultra-relativistic Heavy Ion Collisions," Duke University Report No. DUKE-TH-93-46, 1993 (unpublished).
[7] K. Geiger, Phys. Rev. D **46**, 4965 (1992).
[8] K. Geiger, Phys. Rev. D **46**, 4986 (1992).
[9] K. Geiger, Phys. Rev. D **47**, 133 (1993).
[10] J. D. Bjorken, Phys. Rev. D **27**, 140 (1983).
[11] L. D. Landau, Izv. Akad. Nauk. SSSR, Ser. Fiz. **17**, 51 (1953).
[12] M. Gyulassy and T. Matsui, Phys. Rev. D **29**, 419 (1984); K. Kajantie, R. Raitio, and P. V. Ruuskanen, Nucl. Phys. **B222**, 152 (1983); G. Baym, B. L. Fryman, J.-P. Blaizot, M. Soyeur, and W. Czyz, *ibid.* **A407**, 541 (1983); H. Gersdorff, L. D. McLerran, M. Kataja, and P. V. Ruuskanen, Phys. Rev. D **34**, 794 (1986); N. S. Amelin, E. F. Straubo, L. P. Csernai, V. D. Toneev, K. K. Gudima, and D. D. Strottman, Phys. Rev. Lett. **67**, 1523 (1991).
[13] E. V. Shuryak, Phys. Rev. Lett. **68**, 3270 (1992).
[14] S. de Groot, W. A. van Leuwen, and C. G. van Weert,

Relativistic Kinetic Theory (North-Holland, Amsterdam, 1980).

[15] One has to keep in mind that in the ratios (29) the densities $n^{(\mathrm{eq})}$ and $\varepsilon^{(\mathrm{eq})}$ are evaluated assuming the partons to be on mass shell and neglecting any interactions among them. The actual parton densities n and ε in the numerator on the other hand, include implicitly contributions from "heavier" partons with timelike virtualities, and the effect of parton interactions.

[16] We note that because of the nonvanishing baryon number in the central region (cf. Sec. IV) the densities of u and d quarks should actually be compared to the equilibrium densities with $\mu_a > 0$, taking into account the initial surplus of quarks over antiquarks. In this case the values of the equilibrium densities would be larger than at $\mu_a = 0$ and would reduce the values of $\rho_a^{(n)}$ and $\rho_a^{(\varepsilon)}$ in (32). Therefore, for the light quarks, the quantities (32) might even overestimate slightly the degree of chemical equilibration.

[17] *Quark Gluon Plasma Signatures*, Proceedings of the International Workshop on Quark Gluon Plasma Signatures, Strasbourg, France, 1991, edited by V. Bernard *et al.* (Editions Frontières, Gif-sur-Yvette, France, 1991); C. P. Singh, Int. J. Mod. Phys. A **29**, 7185 (1992).

[18] E. V. Shuryak, Phys. Lett. **78B**, 150 (1978); Yad. Fiz. **28**, 796 (1978) [Sov. J. Nucl. Phys. **28**, 408 (1978)].

[19] B. Müller and X.-N. Wang, Phys. Rev. Lett. **68**, 2437 (1992).

[20] A. Shor, Phys. Lett. B **215**, 375 (1988); **233**, 231 (1989).

[21] P. Koch, B. Müller, and J. Rafelski, Phys. Rep. **142**, 167 (1986).

[22] J. Kapusta and A. Mekjian, Phys. Rev. D **33**, 1304 (1986); T. Matsui, B. Svetitsky, and L. D. McLerran, *ibid.* **34**, 783 (1986); **34**, 2047 (1986).

[23] K. Kajantie and H. Miettinen, Z. Phys. C **9**, 341 (1981); L. D. McLerran and T. Toimela, Phys. Rev. D **31**, 545 (1985); R. C. Hwa and K. Kajantie, *ibid.* **32**, 1109 (1985); K. Kajantie, M. Kataja, L. D. McLerran, and P. V. Ruuskanen, *ibid.* **34**, 811 (1986); J. Kapusta, L. D. McLerran, and D. K. Srivastava, Phys. Lett. B **283**, 145 (1992).

[24] K. Geiger and J. Kapusta, Phys. Rev. Lett. **70**, 1920 (1993).

[25] E. Shuryak and L. Xiong, Phys. Rev. Lett. **70**, 2241 (1993); B. Kämpfer and O. P. Pavlenko, Phys. Lett. B **289**, 127 (1992); I. Kawrakow and J. Ranft, Report No. UL-HEP-92-08, 1992 (unpublished).

[26] K. Geiger, "Strangeness, Charm and Bottom Production from Dense Parton Matter in High Energy Nuclear Collisions," University of Minnesota Report No. NUC-MINN-93/5-T, 1993 (unpublished).